ELSEVIER

International Journal of Heat and Fluid Flow 19 (1998) 470–481

International Journal of HEAT AND FLUID FLOW

DNS study of turbulence modification with streamwise-uniform sinusoidal wall-oscillation

Yoichi Mito *, Nobuhide Kasagi

Department of Mechanical Engineering, The University of Tokyo, 7-3-1, Hongo, Bunkyo-ku, Tokyo 113-8656, Japan

Abstract

In pursuit of a possible active feedback turbulence control method utilizing a flexible wall, a simple oscillatory mode of wall deformation is tested in a turbulent channel flow using direct numerical simulation. The deformation is uniform in the streamwise direction and spatio-temporally sinusoidal, and its parametric conditions are determined with reference to the mean spatio-temporal scales of the quasi-coherent turbulent structures. The effects of the wall deformation on the skin friction as well as on the statistical quantities and turbulent structures are studied. Among the parameters of the wall deformation, the spanwise wavelength and gradient are more effective for the alterations of the skin friction and statistical quantities. The scales of turbulent structures are found to be dependent on the spanwise wavelength of the wall deformation at both their enhanced and damped phases, whereas a spanwise shift of these structures is observed to be correlated with the time period of deformation. The production of turbulent structures becomes highly intermittent on imposing the wall deformation condition, which is similar to that observed in the temporal evolution of the skin friction coefficient as its long-period fluctuation. © 1998 Elsevier Science Inc. All rights reserved.

Keywords: Turbulence modification; Direct numerical simulation; Channel flow; Wall deformation

Notation

a	amplitude of wall deformation
C_{f1}, C_{fT}	skin friction coefficients averaged over the deformed wall and the two walls, respectively
$C_{f\_unactuated}$	skin friction coefficient of the unactuated channel
D^i	divergence operator
$G^i(p)$	pressure gradient terms of Navier–Stokes equations
$\boldsymbol{g}^i$	contravariant base vector
J	Jacobian of coordinate transformation
k	kinetic energy
$L^i(\boldsymbol{q})$	linear terms of Navier–Stokes equations
$N^i(\boldsymbol{q})$	nonlinear terms of Navier–Stokes equations
n	wall-normal direction
p	pressure
Q	total flow rate
$\boldsymbol{q}$, q^i	volume flux vector and its components
$\hat{\boldsymbol{q}}$, $\boldsymbol{q}^*$	intermediate vector functions of a fractional-step method
$Re_{\tau 1}$, $Re_{\tau T}$	Reynolds numbers $u_{\tau 1}\delta/\nu$ and $u_{\tau T}\delta/\nu$, respectively
s	spanwise wavelength of wall deformation
t	time
$T^i(\boldsymbol{q})$	moving coordinate terms of Navier–Stokes equations
T	time period of wall deformation
$\boldsymbol{u}$	velocity vector
u, v, w	velocity fluctuations in the streamwise, wall-normal and spanwise directions, respectively
U_b	bulk-averaged velocity
u_τ	friction velocity of the unactuated channel
$u_{\tau 1}$, $u_{\tau T}$	friction velocity averaged over the deformed wall and the two walls, respectively
$\boldsymbol{v}_g$	velocity of coordinate system
$x_1(x)$, $x_2(y)$, $x_3(z)$	streamwise, wall-normal and spanwise directions, respectively
y_w, z_w	wall displacement in the wall-normal and spanwise directions, respectively

Greek

δ	channel half-width
Δp_1	pressure drop in the streamwise direction
Δt	computational time step
ΔT	time span of averaging
Δx_1, Δx_3	computational grid spacings in the streamwise and spanwise directions, respectively
Γ_w, Γ_{w0}	instantaneous wall surface area and its projection onto the x_1–x_3 plane, respectively
λ	mean spanwise spacing of low-speed streaks
ν	kinematic viscosity
ρ	density
τ_w	local streamwise wall-shear stress
ϕ	scalar function of a fractional-step method

* Corresponding author. Present address: National Aerospace Laboratory, 7-44-1, Jindaiji-higashi, Chofu, Tokyo 182-8522, Japan. E-mail: mito@nal.go.jp.

0142-727X/98/$ – see front matter © 1998 Elsevier Science Inc. All rights reserved.
PII: S0142-727X(98)10025-5

φ	ratio of actuating power input to main flow pumping power
ω_x, ω_y, ω_z	vorticity fluctuations in the streamwise, wall-normal and spanwise directions, respectively

Indices

a^n	quantity in the n-th time step, t^n
a^+	quantity non-dimensionalized by u_τ and ν
a_{rms}	root-mean-square value

1. Introduction

Technological benefits such as skin friction reduction and heat transfer augmentation can be often achieved by turbulence modification, particularly by altering the turbulent coherent structures, which are known to play central roles in the turbulent transport mechanism. In order to reduce skin friction, Jung et al. (1992) applied spanwise wall oscillations and Choi et al. (1994) employed local wall blowing and suction to turbulent channel flows in their recent direct numerical simulations (DNS, hereafter). Both of these methods successfully suppressed the turbulence-producing structures. Turbulent heat transfer can be augmented by using various kinds of vortex generators (Jacobi and Shah, 1995) and roughness elements (Webb, 1987), both of which are installed to intensify the vortical structures and enhance turbulence mixing. Among various modes of flow actuation, active wall deformation can be a plausible method for engineering applications. The purpose of this work is to examine the effects of a relatively simple wall oscillation mode on the turbulent structures of a canonical wall-bounded shear flow, as well as on the skin friction and statistical quantities.

At present, using DNS, a turbulence modification scheme has been tested in a plane channel, one of the two walls of which is subject to deformation. The mode of oscillatory deformation is assumed to be uniform in the streamwise direction and spatio-temporally sinusoidal. This assumption reduces the number of parameters prescribed for the flow control and facilitates a parametric analysis. Streamwise uniformity of the wall deformation is desired for its possible interaction with the turbulent structures which are elongated or long-lived in the streamwise direction without additional streamwise pressure drag possibly caused by a streamwise component of the wall deformation. In this work, the discussion is limited to the modification of turbulent momentum transport, although scalar transport is also of great interest. The alteration of skin friction, statistics and turbulent structures is studied in order to explore the relation between the parameters of wall deformation and the resultant influences.

2. Numerical schemes

DNS has been extensively used for understanding the fundamental physics of turbulent shear flows (see, e.g., Moin and Spalart, 1989; Kasagi and Shikazono, 1995). Among various kinds of discretization schemes the most prevailing means for DNS, which can also be applied to a general flow geometry, is to utilize a fractional-step method (Chorin, 1969; Temam, 1984) and a finite difference method for the temporal and spatial discretizations, respectively. The solution of the fractional-step method can be linearized and accelerated by a semi-implicit method, i.e., a combination of an implicit method for the viscous diffusion terms and an explicit method for the other terms (Chorin, 1969; Kim and Moin, 1985). Presently, a modified Crank–Nicolson type fractional-step method (Choi and Moin, 1994), which adopts a more accurate and stable trapezoidal integration scheme with a delta-form of the pressure gradient terms is used to suppress the temporal phase error encountered in a semi-implicit method and to precisely reflect the influence of wall deformation in DNS.

The governing equations are the incompressible Navier–Stokes equations and the continuity equation. The wall deformation is described with a boundary-fitted coordinate system. Thus the calculation of the computational grid and its metrics is performed at each time step. The volume flux components, which correspond to the contravariant components multiplied by the Jacobian of the coordinate transformation, are chosen for the momentum equations.

$$J\boldsymbol{g}^i \cdot \left(\frac{\partial \boldsymbol{u}}{\partial t} + \left[(\boldsymbol{u} - \boldsymbol{v}_g) \cdot \nabla \right] \boldsymbol{u} + \frac{1}{\rho} \nabla p - \nu \nabla^2 \boldsymbol{u} \right) = 0, \tag{1}$$

where $\boldsymbol{v}_g$ indicates the velocity of the coordinate system in the physical domain. The continuity equation is given by

$$\nabla \cdot \boldsymbol{u} = 0. \tag{2}$$

Eq. (1) is rewritten as follows for brevity:

$$\frac{\partial q^i}{\partial t} = T^i(\boldsymbol{q}) + N^i(\boldsymbol{q}) - G^i(p) + L^i(\boldsymbol{q}), \quad (i = 1, 2, 3), \tag{3}$$

where:

$$T^i(\boldsymbol{q}) = \boldsymbol{u} \cdot \frac{\partial}{\partial t} J\boldsymbol{g}^i + J\boldsymbol{g}^i \cdot \left(\boldsymbol{v}_g \cdot \nabla \right) \boldsymbol{u}, \tag{4}$$

$$N^i(\boldsymbol{q}) = -J\boldsymbol{g}^i \cdot (\nabla \cdot \boldsymbol{u}\boldsymbol{u}), \tag{5}$$

$$G^i(p) = \frac{J}{\rho} \boldsymbol{g}^i \cdot \nabla p, \tag{6}$$

$$L^i(\boldsymbol{q}) = \nu J\boldsymbol{g}^i \cdot \nabla^2 \boldsymbol{u}. \tag{7}$$

By considering the temporal phase of each operator in the fractional-step method, the modified Crank–Nicolson type fractional-step method is extended to a moving coordinate system as follows:

$$\frac{\hat{\boldsymbol{q}} - \boldsymbol{q}^n}{\Delta t} = \frac{1}{2} \left(\boldsymbol{T}^{n+1}(\hat{\boldsymbol{q}}) + \boldsymbol{T}^n(\boldsymbol{q}^n) \right) + \frac{1}{2} \left(\boldsymbol{N}^{n+1}(\hat{\boldsymbol{q}}) + \boldsymbol{N}^n(\boldsymbol{q}^n) \right) + \frac{1}{2} \left(\boldsymbol{L}^{n+1}(\hat{\boldsymbol{q}}) + \boldsymbol{L}^n(\boldsymbol{q}^n) \right) - \boldsymbol{G}^n(\phi^n), \tag{8}$$

$$\frac{\boldsymbol{q}^* - \hat{\boldsymbol{q}}}{\Delta t} = \boldsymbol{G}^n(\phi^n), \tag{9}$$

$$\frac{\boldsymbol{q}^{n+1} - \boldsymbol{q}^*}{\Delta t} = -\boldsymbol{G}^{n+1}(\phi^{n+1}). \tag{10}$$

In the above equations, $\boldsymbol{q}$, $\hat{\boldsymbol{q}}$ and $\boldsymbol{q}^*$ are the volume flux (Rosenfeld et al., 1991) and two intermediate vector functions, respectively. The superscript indices, n and $n+1$, denote the reference time steps, t^n and t^{n+1}. The scalar function of ϕ^{n+1} in Eq. (10) can be solved by the following equation,

$$(D^i G^i)^{n+1}(\phi^{n+1}) = \frac{1}{\Delta t} D^{i^{n+1}} q^{*i}, \tag{11}$$

where D^i is a divergence operator defined by

$$\nabla \cdot \boldsymbol{u} \equiv D^i q^i. \tag{12}$$

The continuity equation is used in the derivation of Eq. (11).

A second-order finite difference scheme is used for the spatial discretization of both flow variables and metrics. A staggered mesh system is used with additional grid points near the wall to preserve the interpolative discretization scheme. To maintain second-order accurate distributions, biased interpolative discretization schemes are used near the wall. For the staggered mesh system, second-order accurate interpolations are necessary in the convective term for a conservative form. In the channel core region, a diagonal 8-point scheme is used for the planar interpolation to preserve symmetry discretization, whereas a 12-point scheme is used for the planar interpolation

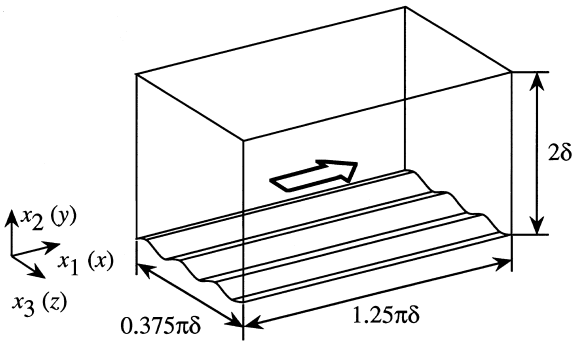

Fig. 1. Flow geometry and coordinate system.

in the near-wall region with a one-dimensional 3-point scheme in the wall-normal direction and a one-dimensional 4-point scheme in the streamwise or spanwise direction. Eqs. (8) and (11) are solved by a Newton method combined with an approximate factorization technique (Choi et al., 1992), and by an incomplete LU conjugate gradient squared (ILUCGS) method and a fast Fourier transform algorithm, respectively.

The flow geometry and the coordinate system are shown in Fig. 1. A fully developed turbulent channel flow is assumed, and periodic boundary conditions are used in the streamwise (x_1) and spanwise (x_3) directions. The simulation is performed under the constant flow rate condition throughout the present study. The Reynolds number is 4600 based on the bulk mean velocity U_b and the channel width 2δ (about 150 based on the friction velocity and the channel half-width for the unactuated turbulent channel flow). Hereafter, u_τ represents the friction velocity in the unactuated channel flow, while all the parameters with a superscript + represent quantities non-dimensionalized by u_τ and the kinematic viscosity ν.

The size of the computational volume is 1.25 $\pi\delta$ in the streamwise direction and 0.375 $\pi\delta$ in the spanwise direction, which correspond to about 590 and 180 ν/u_τ, respectively. It is about 2.5 and 1.5 times larger than the so-called minimal flow unit (Jiménez and Moin, 1991). The number of grid points is 48, 97 and 48 in the x_1, x_2 and x_3 directions, respectively. Uniform meshes are used in the streamwise and spanwise directions with spacings $\Delta x_1^+ = 12$ and $\Delta x_3^+ = 3.7$, respectively. A non-uniform mesh with a hyperbolic tangent distribution is used in the x_2 direction. The first mesh point away from the wall is given at $x_2^+ = 0.25$. The computational time step is $0.33\ \nu/u_\tau^2$. An instantaneous flow field of a fully developed turbulent channel flow was used for the initial condition. After an initial period of $1300\ \nu/u_\tau^2$, statistical averages over a time span of $6500\ \nu/u_\tau^2$ were calculated for each case.

3. Wall deformation mode

In the present study, one side wall is actuated, while the other is kept flat and stationary. The streamwise uniform wall displacement (y_w, z_w) is given by:

$$y_w = a \sin\frac{2\pi z}{s}\sin\frac{2\pi t}{T}, \quad z_w = 0, \tag{13}$$

where a, s and T are the amplitude, spanwise wavelength and time period of the wall oscillation, respectively, as shown in Fig. 2. With this deformation mode, the cross sectional area of the channel is kept constant. We focus on the possibility of effective turbulence control acting on turbulent coherent structures, particularly on the longitudinal vortical structures, so that the values of the above parameters are specified by

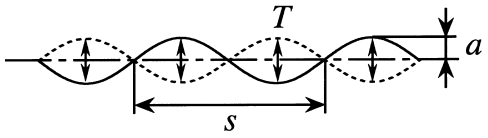

Fig. 2. Wall deformation mode.

referring to their typical scales (Robinson, 1991), e.g., the mean spanwise spacing of low-speed streaks, $\lambda = 100\ \nu/u_\tau$ (Smith and Metzler, 1983), the mean diameter of longitudinal vortices, $30\ \nu/u_\tau$ (Kim et al., 1987), and the mean rotational time period of longitudinal vortices, $80\ \nu/u_\tau^2$ deduced from its mean circulation, $80\ \nu$ (Robinson, 1991).

As listed in Table 1, two spanwise wavelengths are chosen: $s^+ = 90$, which is almost equal to λ, and $s^+ = 45$, which is almost equal to the diameter of vortices. Similarly, but based on the time scale of longitudinal vortices, two time periods are also selected: $T^+ = 50$ and 100. The oscillatory amplitudes are assumed to be $a^+ = 2.5$ and 5.0, which are comparable with the thickness of the viscous sublayer. This final assumption has come from an observation that the seeds of turbulence-producing eddies, i.e., longitudinal vortices, lie in the viscous region close to the wall (Brook and Hanratty, 1993). Thus, the present mode and parameters for wall deformation have been designed so that the origin or the initial stage of evolution of the turbulence-producing eddies should be a major control target.

4. Skin friction

The skin friction coefficient on the deformed wall, C_{f1}, and the mean skin friction coefficient averaged over the two walls, C_{fT}, are summarized in Table 2. The former is defined as follows:

$$C_{f1} = \left[\frac{1}{\Delta T}\int_{\Delta T} \mathrm{d}t \cdot \int_{\Gamma_w} \tau_w \,\mathrm{d}\Gamma/\Gamma_{w0}\right] \Big/ \left(\rho U_b^2/2\right), \tag{14}$$

where ΔT, Γ_w, Γ_{w0} and τ_w denote the time span of averaging, the instantaneous wall surface area, its projection onto the $x_1 - x_3$ plane and the local streamwise wall-shear stress on the deformed wall, respectively. In Table 2, the two Reynolds numbers are also included: $Re_{\tau 1}$ and $Re_{\tau T}$, based on the friction on the deformed wall and the mean friction averaged over the two walls, respectively. Presently, three kinds of secondary parameters are calculated as shown in Table 2: i.e., a^+/s^+, a^+/T^+ and $a^{+2}/T^+ s^+$, which characterize the gradient, the velocity and the strain rate associated with the wall deformation, respectively. The third parameter can also be considered as specific streamwise vorticity on the deformed wall. The ratios of the skin friction coefficients on the deformed walls and those in the unactuated case are shown in Fig. 3.

When the same flow rate is given by a laminar flow, the skin friction coefficient is 2.59×10^{-3}. For the present range of parameters, a small amount of skin friction reduction on the deformed wall is achieved at $(s^+, T^+, a^+) = (45, 50, 2.5)$, (90, 50, 5.0) and (90, 100, 5.0). In comparison with the results of wavy channels, i.e., the cases of stationary wall deformation,

Table 1
Wall deformation parameters

s^+	T^+	a^+
45, 90	50, 100	2.5, 5.0

Table 2
Skin friction coefficients

s^+	T^+	a^+	a^+/s^+	a^+/T^+	a^{+2}/T^+s^+	C_{f1}	$Re_{\tau 1}$	C_{fT}	$Re_{\tau T}$
Unactuated			–	–	–	–	–	8.53×10^{-3}	151
45	–	5.0	0.113	–	–	9.74×10^{-3}	162	9.27	158
	50	2.5	0.057	0.048	2.7×10^{-3}	8.46	151	8.55	152
		5.0	0.113	0.096	10.8	8.71	153	8.59	152
	100	2.5	0.057	0.026	1.4	8.64	152	8.51	151
		5.0	0.113	0.051	5.8	9.20	157	8.90	155
90	–	5.0	0.057	–	–	9.24	158	8.97	155
	50			0.096	5.4	8.46	151	8.48	151
	100			0.051	2.9	8.46	151	8.60	152

it is clear that the skin friction can be reduced only by imposing a temporal effect on the wall deformation within the present range of parameters. This temporal effect of wall deformation contains not only a local pushing or pulling mode but also a shifting mode in the spanwise direction as shown later. Conversely, the skin friction is most enhanced at (s^+, T^+, a^+) = (45, 100, 5.0) although the value is still smaller than those of the wavy channels. Clear dependence of the skin friction on a^+/s^+ is observed, i.e., the skin friction becomes larger in the case of $a^+/s^+ = 0.113$ than in the case of $a^+/s^+ = 0.057$, whereas no correlation is observed between the skin friction and the other two secondary parameters. The spanwise wavelength s^+ is also correlated with the skin friction except in the case of (s^+, T^+, a^+) = (45, 50, 2.5), i.e., the skin friction becomes larger for the cases with $s^+ = 45$ than for the cases with $s^+ = 90$. The exception might reflect the difference in the amplitudes a^+, i.e., the parametric tendency of the skin friction might be changed by the extent of intrusion of the wall deformation into turbulence. Hence, the following comparison and discussion are restricted to the cases of $a^+ = 5.0$, with which the skin friction is altered distinctly.

For the present wall deformation modes, the ratio of actuating power input to the main flow pumping power, φ, is defined as:

$$\varphi = -\int_{\Gamma_w} \left(u_n k + u_n p - \frac{1}{\mathrm{Re}} \frac{\partial k}{\partial n} \right) \mathrm{d}\Gamma \, / Q \Delta p_1, \tag{15}$$

where k, Δp_1, Q and n denote the kinetic energy, the pressure drop in the streamwise direction, the total flow rate and the wall-normal direction, respectively. The above ratio is about 1% at the instantaneous maximum in the case of (s^+, T^+, a^+) = (90, 50, 5.0), but all the averaged values are found to be about 0.1%. Thus, the extra power input for the present turbulence modification remains negligible.

5. Statistics

The time-averaged statistics have been obtained by interpolating data at each distance from the mean height of the deformed wall. The one-dimensional third-order (4-point) and second-order (3-point) interpolations are used in the channel-core and near-wall regions, respectively. Thus, the local zones covered by the wall deformation are excluded from the averaging.

The mean velocity profiles on the deformed walls are shown in Fig. 4. In all cases with wall deformation, the mean flows are decelerated by almost the same extent compared with the unactuated case, although there are obvious differences in the skin friction coefficients as shown in Table 2. The shift of the virtual origin is based on the increased displacement of the wall flow by imposing the wall deformation. The skin friction alteration among these profiles may be caused by the ex-

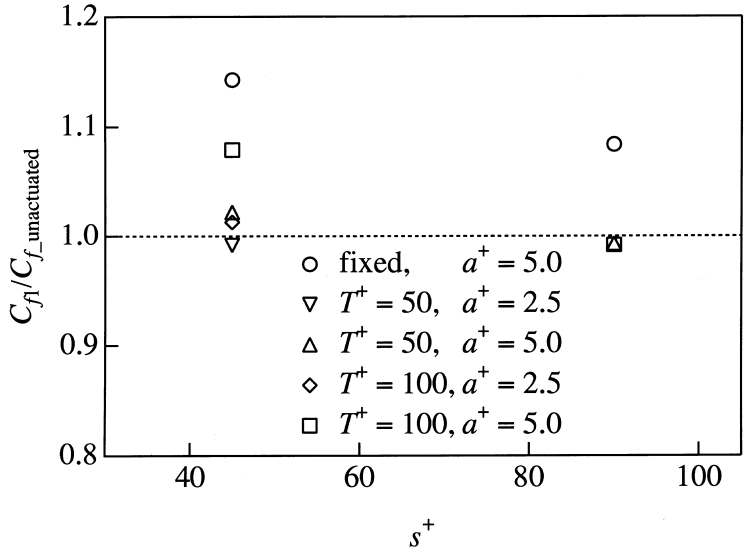

Fig. 3. Ratios of the skin friction coefficients on the deformed walls and that in the unactuated case.

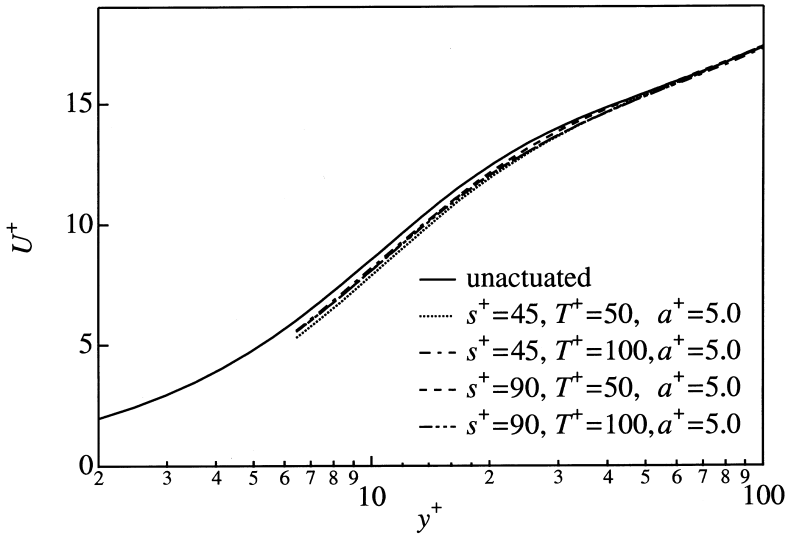

Fig. 4. Mean velocity profiles.

tent of clustering of the high wall-shear regions on the deformed wall.

Figs. 5–7 show the distributions of root-mean-square velocity fluctuations on the deformed wall. Although little difference is observed in the streamwise velocity fluctuations (Fig. 5), this component becomes larger in the case of $s^+ = 45$ than in the case of $s^+ = 90$ above the buffer region. In these two cases, the skin friction has been likewise enhanced and reduced, respectively, as shown in Table 2.

The wall-normal (Fig. 6) and spanwise (Fig. 7) components are much enhanced in the case of (s^+, T^+, a^+) = (45, 100, 5.0) and reduced in the case of (s^+, T^+, a^+) = (90, 100, 5.0), for which the skin friction has been similarly enhanced and reduced, respectively. In the near-wall region, the wall-normal velocity fluctuations become larger than the unactuated case in accordance with the velocity component of wall deformation. Thus this component becomes still larger in the case of $T^+ = 50$ than in the case of $T^+ = 100$ because of the definition of wall deformation shown in Eq. (13). Except for the near-wall region, this component in the case of $T^+ = 50$ almost agrees with the unactuated case. Since the wall-normal velocity fluctuation corresponds to the actuating component of the wall deformation, these observations indicate that the wall deformation of $T^+ = 50$ cannot directly affect the wall-normal velocity component whereas the wall deformation of (s^+, T^+, a^+) = (45, 100, 5.0) and (90, 100, 5.0) could directly enhance and attenuate the wall-normal velocity component, respectively. This tendency is also reflected in the spanwise velocity fluctuations as the redistributed component.

The increase and decrease of the wall-normal velocity fluctuations are also reflected in the Reynolds shear stress distributions on the deformed walls as shown in Fig. 8. In the case of the increased skin friction when (s^+, T^+, a^+) = (45, 100, 5.0), the Reynolds shear stress is markedly increased, whereas it is decreased in the case of the reduced skin friction when (s^+, T^+, a^+) = (90, 100, 5.0). The same tendency is likewise observed in the cases of (s^+, T^+, a^+) = (45, 50, 5.0) and (90, 50, 5.0), in which the skin friction increases and reduces,

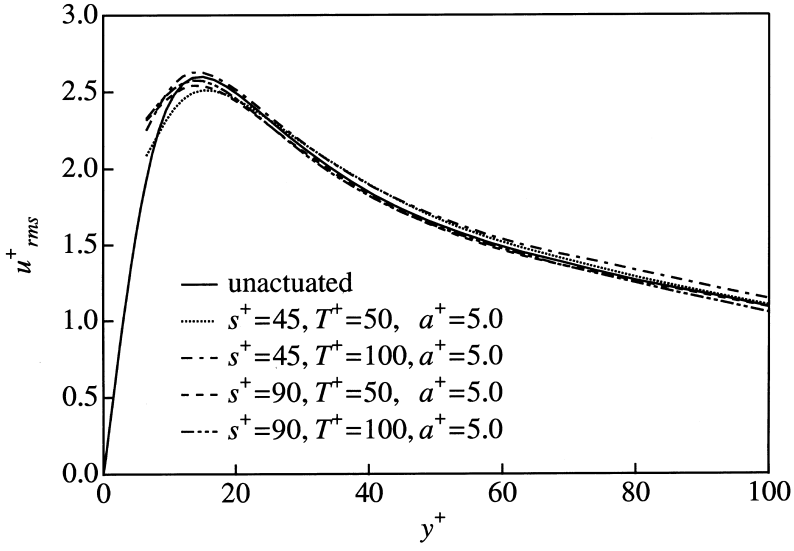

Fig. 5. RMS streamwise velocity fluctuations.

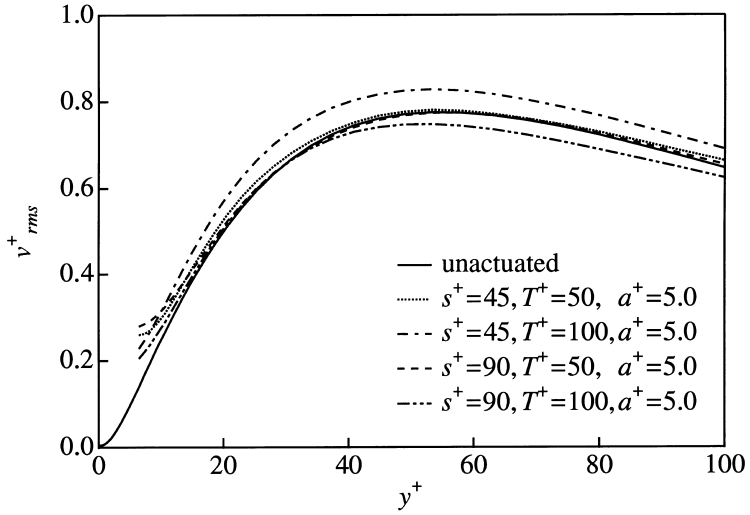

Fig. 6. RMS wall-normal velocity fluctuations.

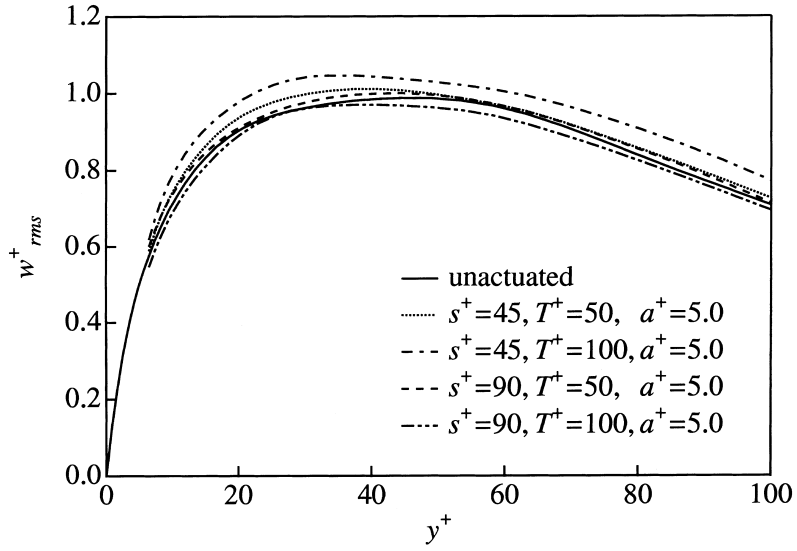

Fig. 7. RMS spanwise velocity fluctuations.

respectively, however, the extent of the increase or decrease is smaller than the cases of $T^+ = 100$, as similarly observed in the cross-sectional velocity fluctuations.

The streamwise vorticity fluctuations on the deformed wall are shown in Fig. 9. This component corresponds to the actuating component of the wall deformation, so that its distribution reflects the receptivity or sensitivity of the induced flow structures to the disturbances brought on by the wall deformation. In the cases of the increased skin friction when (s^+, T^+, a^+) = (45, 50, 5.0) and (45, 100, 5.0), the streamwise vorticity fluctuations on the deformed wall are increased, whereas they almost agree with the unactuated case in the cases of the reduced skin friction when (s^+, T^+, a^+) = (90, 50, 5.0) and (90, 100, 5.0). In the latter cases, larger receptivity to the disturbances caused by the wall deformation can be observed than in the former cases. This fact might mean that the skin friction could be reduced in the case of larger receptivity and vice versa.

The wall-normal vorticity fluctuations on the deformed wall are shown in Fig. 10. This component typically shows the spanwise gradient of the streamwise velocity fluctuation because of the streamwise uniform configuration of the flow field. The wall-normal vorticity fluctuations become large in the cases of the increased skin friction when (s^+, T^+, a^+) = (45, 50, 5.0) and (45, 100, 5.0), whereas they almost agree with the unactuated case in the cases of the reduced skin friction when (s^+, T^+, a^+) = (90, 50, 5.0) and (90, 100, 5.0). Hence the wall-normal vorticity fluctuations are increased by the disturbance due to a smaller pitch.

The spanwise vorticity fluctuations on the deformed wall are shown in Fig. 11. A similar trend as the wall-normal vorticity fluctuations can be observed in the spanwise vorticity fluctuations although this component typically shows the wall-normal gradient of the streamwise velocity fluctuations because of the streamwise uniform configuration of the flow field. This fact implies that the wall bumping of

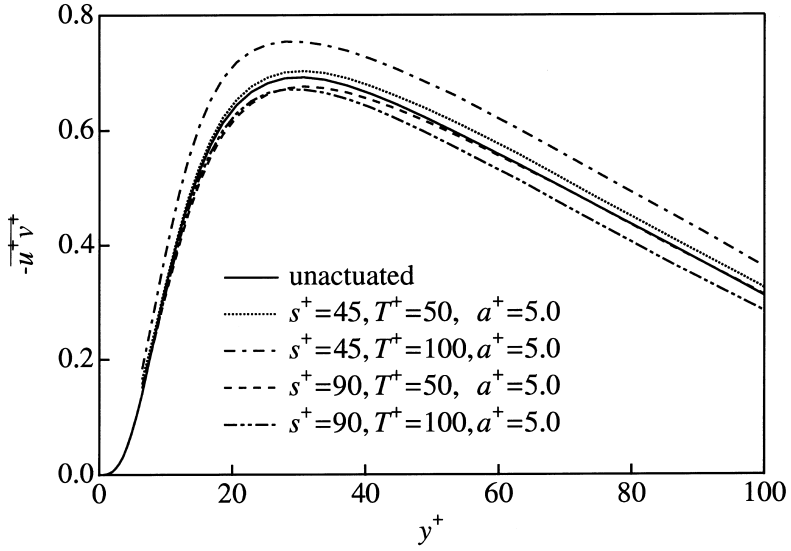

Fig. 8. Reynolds shear stresses.

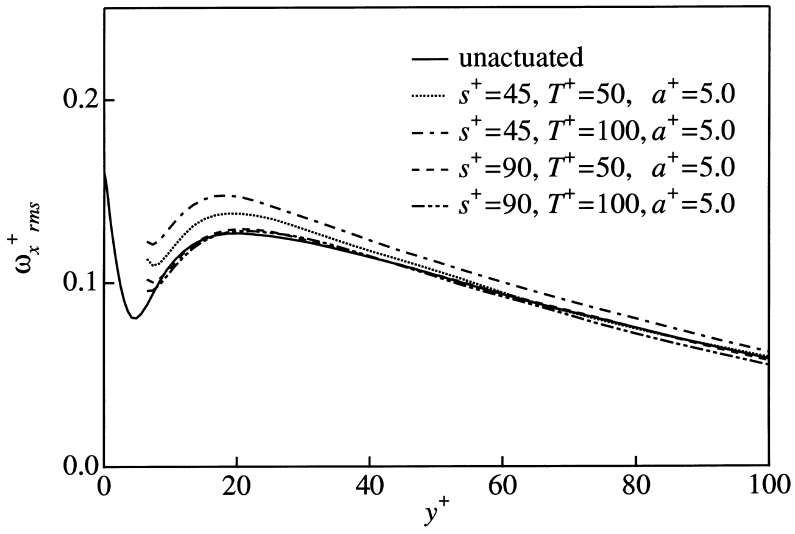

Fig. 9. RMS streamwise vorticity fluctuations.

the smaller pitch often steepens the wall-normal gradient of the streamwise velocity fluctuation and increases skin friction.

6. Temporal evolution

6.1. Skin friction

Fig. 12 shows the initial evolutions of the instantaneous skin friction coefficient on the deformed wall after the wall deformation is started. A fluctuation of the skin friction coefficient caused by the wall deformation is observed. Fig. 13 shows the long-range evolutions of the instantaneous skin friction coefficient on the deformed wall. Each evolution has two fluctuations during each time period of the wall deformation because of the symmetric effects of the former and latter halves of the wall deformation period, and it becomes a local minimum at the phase of zero displacement and local maximum at the phase of maximum displacement. The amplitude of the fluctuation of the skin friction coefficient becomes larger in the case of the smaller spanwise wavelength $s^+ = 45$ than in the case of the larger wavelength $s^+ = 90$. In addition to the short-period fluctuation shown in Fig. 12, there exists a long-period fluctuation in the evolution of the skin friction coefficient, which is caused by the structural alteration of turbulence as illustrated by its visualization, (see next section). For the long-period fluctuation, the skin friction coefficient sometimes shows larger variations (both reduction and enhancement) than that exhibited in the unactuated case.

The present wall deformation mode, which is applied continuously to turbulent channel flow, does not prove to be effective in reducing the mean skin friction. For such a purpose, however, the existence of this distinct phase of skin friction reduction suggests a possible implementation of "on-demand" wall deformation instead of a continuous one.

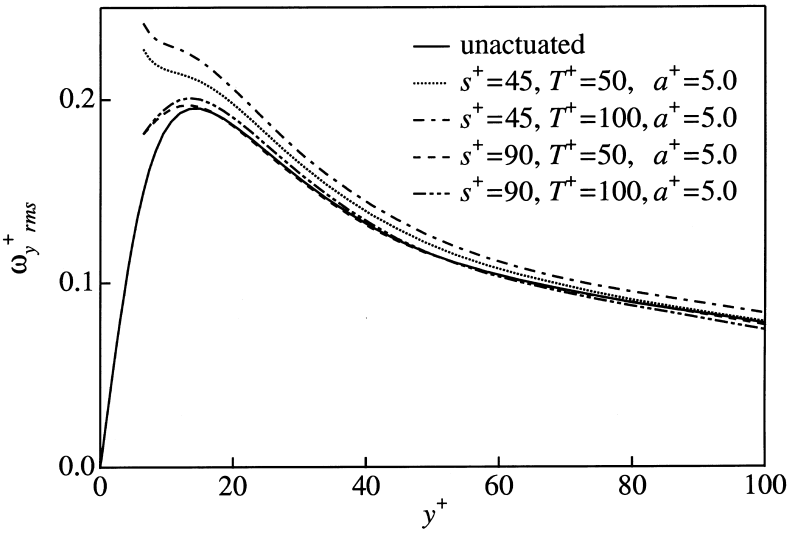

Fig. 10. RMS wall-normal vorticity fluctuations.

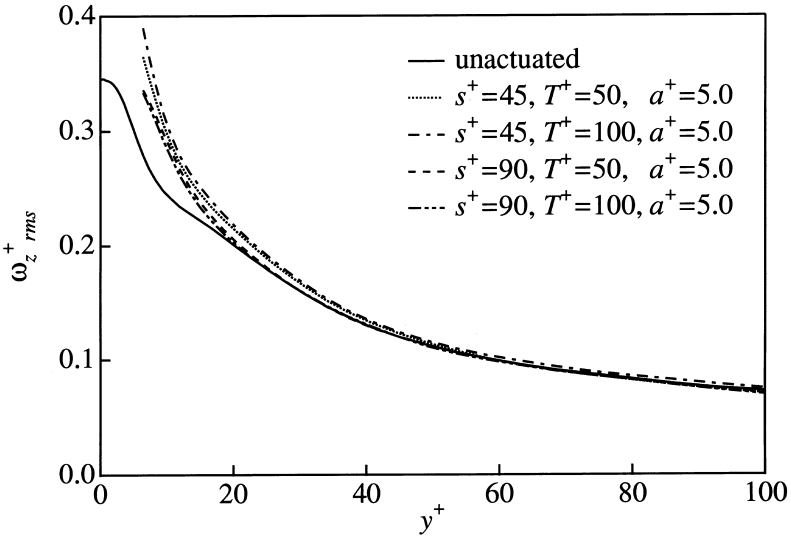

Fig. 11. RMS spanwise vorticity fluctuations.

6.2. Turbulent coherent structures

Fig. 14(a)–(d) show the turbulent structures over the deformed walls at the maximum displacement phase of wall deformation during the periods of increased skin friction. Fig. 14(e) shows the turbulent structures during the period of increased skin friction in the unactuated channel. The time instant for each case is indicated by indices (a)–(e) in Fig. 13. The low-pressure regions, low-speed streaks and high-speed regions are visualized in these figures, where the fluctuations are calculated based on the mean value at the equivalent dimensionless height, $x_2/(2\delta - y_w)$, in the unactuated case. The low-pressure regions mostly correspond to vortex core regions (Robinson, 1991; Kasagi et al., 1995). In these periods, the turbulent structures seem to be much enhanced compared to those visualized in the periods of smaller skin friction. For the smaller spanwise wavelength $s^+ = 45$, i.e., for the larger spanwise gradient a^+/s^+, small-scale turbulent structures are frequently induced and intensified on the deformed walls. This observation is also reflected in the vorticity fluctuations shown in Figs. 9–11.

Typical coherence is observed between the spanwise phase of wall deformation and the turbulent structures, i.e., the high-speed regions often exist above the crest of wall deformation, whereas the low-speed regions frequently lie in the valley. This fact is also illustrated in the wall-shear distributions on the deformed walls shown in Fig. 15. This figure also shows that the high wall-shear regions are more frequently induced in the case of $s^+ = 45$ than in the case of $s^+ = 90$.

The enhanced turbulent structures shown in Figs. 14 and 15 are markedly damped at the periods of reduced skin friction as shown in Fig. 16. Each picture is again taken at the maximum displacement phase of wall deformation. Fig. 16(e′) shows the turbulent structures in the unactuated case. Likewise, the time instant for each case is indicated by indices (a′)–(e′) in Fig. 13. From the comparison of these pictures with those in Fig. 14, it is obvious that the difference between the turbulent structures observed in the periods of the increased and decreased skin

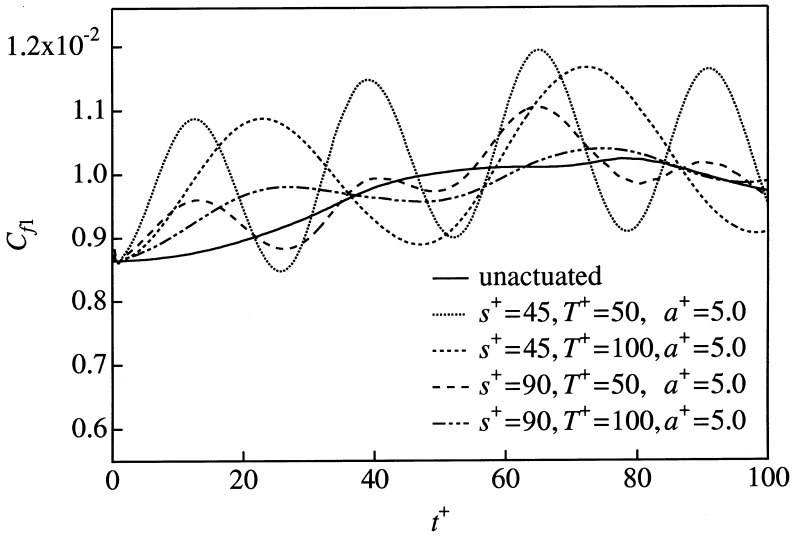

Fig. 12. Evolution of skin friction coefficient in the initial period of flow control.

friction is much larger in the actuated channels than in the unactuated one. In the former, the turbulent energy-producing vortices, denoted as the low-pressure regions, are hardly visible, although the elongated streaky structures are stably formed and well aligned with the streamwise-uniform deformation of the wall. This fact implies that the intermittency

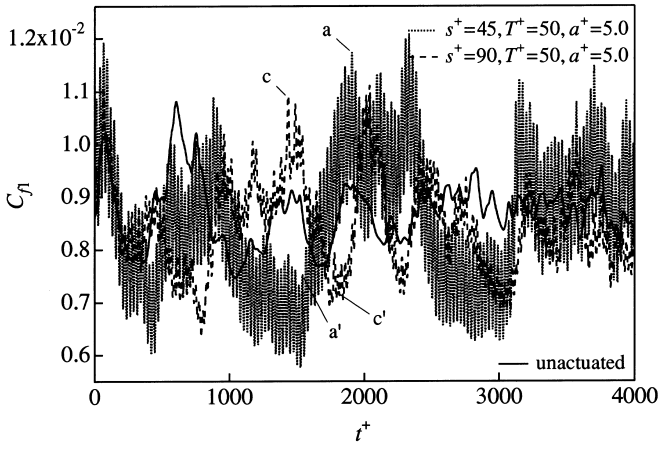

(a) $T^+ = 50$

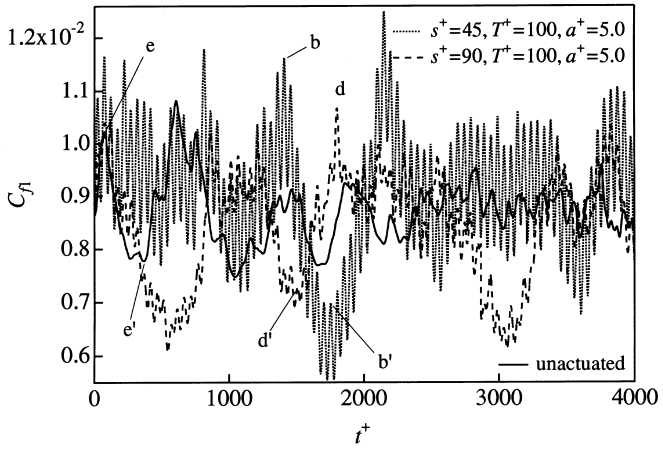

(b) $T^+ = 100$

Fig. 13. Evolution of skin friction coefficient. Indices a–e and a′–e′ represent the time instants of the instantaneous flow fields shown in Figs. 14–16.

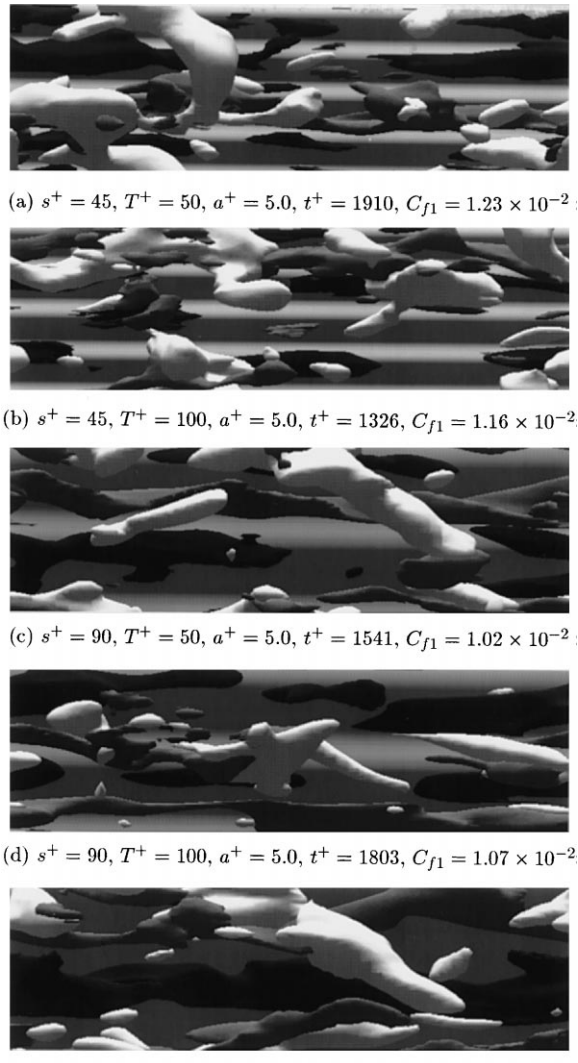

Fig. 14. Turbulent coherent structures on the deformed walls at large skin friction instants shown in Fig. 13. Cases (a)–(d) correspond to the phase of maximum displacement for each wall deformation mode. White: $p^+ = -2.5$, light gray: $u^+ = -3.5$, dark gray: $u^+ = 3.5$.

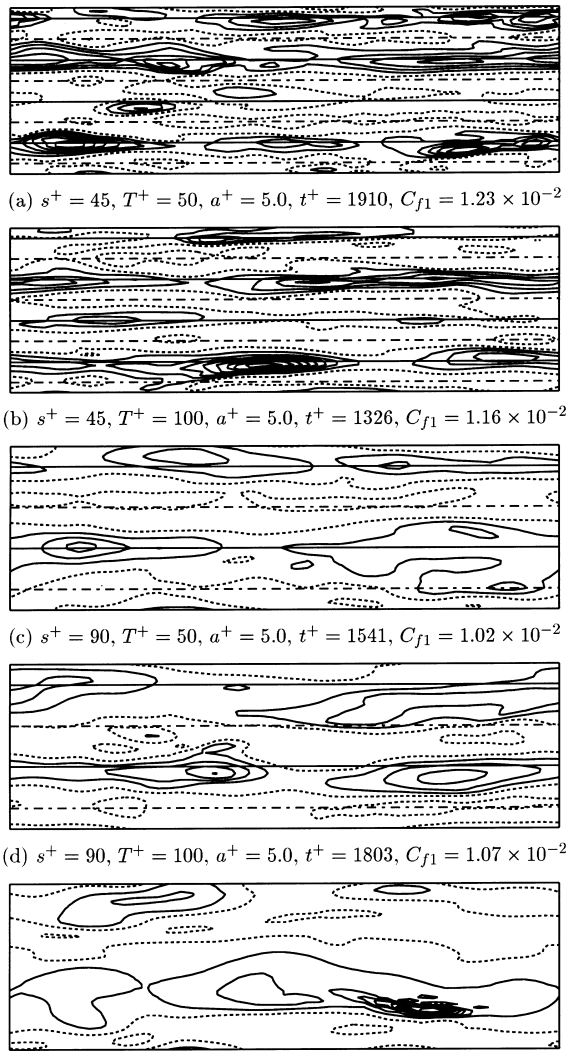

Fig. 15. Wall shear stress τ_w^+ distributions on the deformed walls at the skin friction instants similar to that in Fig. 14. The contour levels range from 0.5 to 5.0 in increments of 0.5. Smaller contours, at 0.5 and 1.0, are dotted. Crests and valleys of wall deformation are also shown by solid and dashed lines, respectively.

of the turbulent structures is increased by the wall deformation, which is reflected in the long-period fluctuation of the skin friction coefficient shown in Fig. 13.

At the initial period of increase in the long-period fluctuation of the skin friction coefficient, an intrusion of high-momentum fluid near the wall as shown in Fig. 17 is initially observed. Stable streaky structures near the wall become unstable with the development of high-speed regions, which causes new vortices to grow with time, and eventually the entire flow field returns to the activated state at the period of increased skin friction.

The time period of the wall deformation causes the shifting of the turbulent structures in the spanwise direction based on the spatial coherence between the spanwise phase of wall deformation and the turbulent structures as mentioned above. The cross sections of the velocity vector distributions are shown in Fig. 18 by the gradation contours of the streamwise velocity fluctuation. Each picture is taken at every quarter of the time period of the wall deformation in the case of (s^+, T^+, a^+) = (45, 100, 5.0). It is observed that the low-speed and high-speed regions are shifted in the spanwise direction depending on the alteration of the deformation phase between the crest and the valley. Thus the temporal effect of the wall deformation enhances meandering of the low-speed streaks and this meandering effect becomes larger in the case of the larger spanwise wavelength of $s^+ = 90$ than in the case of $s^+ = 45$ (not shown). It is noted that the skin friction can be reduced by imposing the temporal parameter for the case of the larger spanwise wavelength $s^+ = 90$, i.e., at the larger meandering effect, in the present range of parameters.

The present DNS showed that the large-scale turbulent structures, which can be observed as a result of the long-period fluctuation of the skin friction coefficient or the large intermittency of the turbulent structures, can be altered by actuating small-scale turbulent structures. The computational volume, however, is too small to realize the large-scale turbulent structures completely, thus this point should be confirmed using DNS of the entire domain.

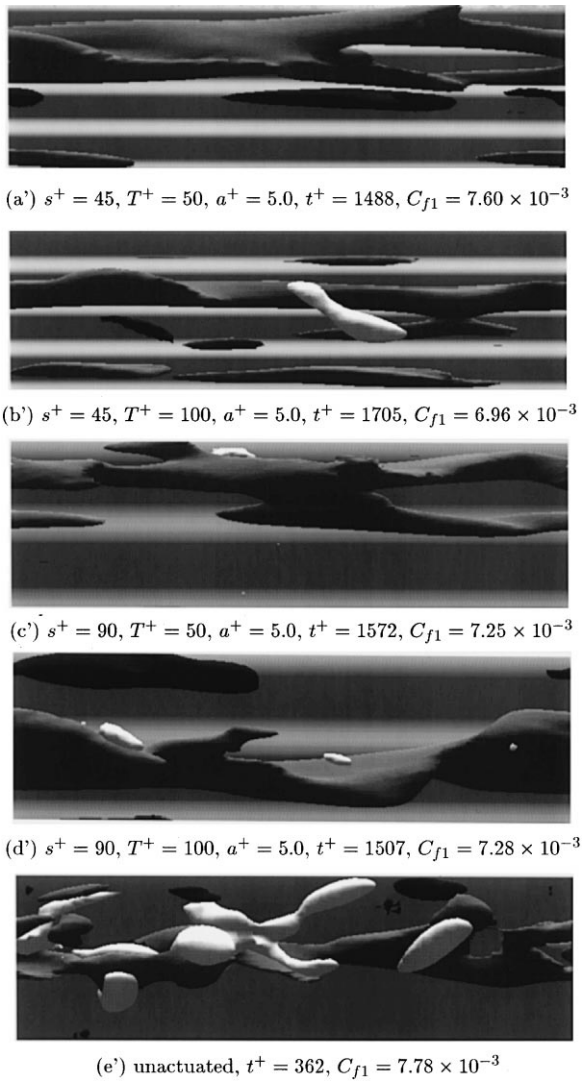

Fig. 16. Turbulent coherent structures on the deformed walls at small skin friction instants shown in Fig. 13. Cases (a′)–(d′) correspond to the phase of maximum displacement for each wall deformation mode. White: $p^+ = -2.5$, light gray: $u^+ = -3.5$, dark gray: $u^+ = 3.5$.

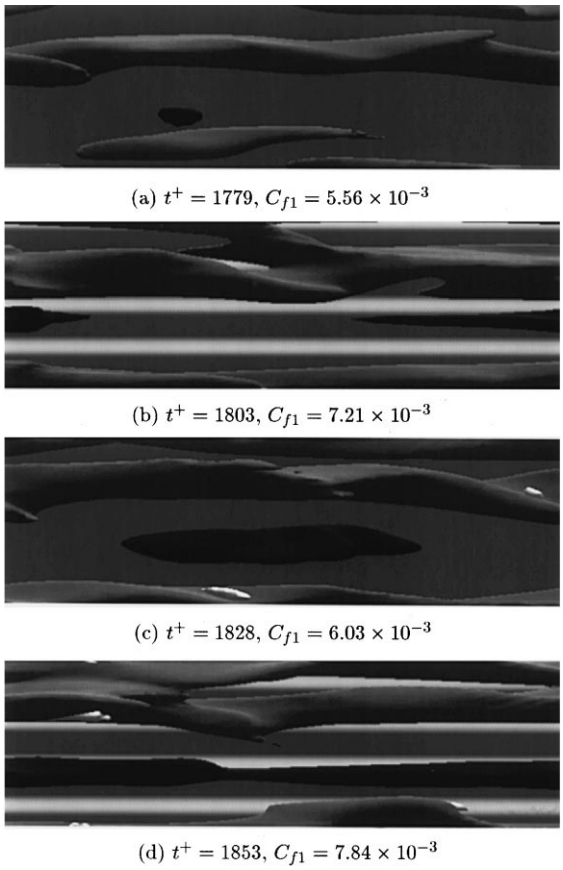

Fig. 17. Turbulent coherent structures on the deformed wall over the period shown in Fig. 13 ($s^+ = 45$, $T^+ = 100$, $a^+ = 5.0$). Cases (a) and (c) correspond to the phase of zero displacement, while cases (b) and (d) correspond to the phase of maximum displacement, respectively. White: $p^+ = -2.0$, light gray: $u^+ = -3.5$, dark gray: $u^+ = 3.5$.

7. Conclusions

Direct numerical simulation of turbulent channel flow with an oscillatory deformed wall has been performed using a temporally rigorous numerical scheme. In the present range of parameters, the spanwise wavelength of the wall deformation is more effective in the skin friction alteration than the time period, while imposing the temporal parameter on the wall deformation which is essential to the skin friction reduction. The

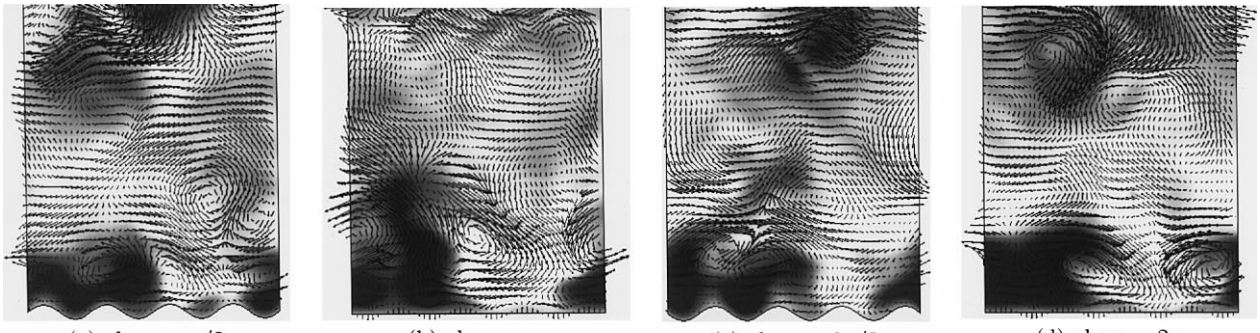

Fig. 18. Cross sections of the velocity vectors and streamwise velocity fluctuations at every quarter of the time period of the wall deformation ($s^+ = 45$, $T^+ = 100$, $a^+ = 5.0$). Black to white: $u^+ = -3.5$ to 3.5.

skin friction change is typically reflected in the vorticity fluctuations and the receptivity of the induced flow structures to disturbances becomes larger in the reduced skin friction case than in the increased skin friction case. The evolution of the skin friction coefficient comprises short-period fluctuations based on the wall deformation and long-period fluctuations based on the alteration of the turbulent structures. Visualization of turbulent structures has illustrated that the scales of turbulent structures are largely dependent on the spatial scales of the wall deformation and that the turbulence becomes highly intermittent. At the initial period of increase in the long-period fluctuation of the skin friction coefficient, an intrusion of high-momentum fluid near the wall is initially observed.

Acknowledgements

This work was supported by the Ministry of Education, Science, Culture and Sports through the Grant-in-Aid for Developmental Scientific Research (No. 08455102).

References

Brook, J.W., Hanratty, T.J., 1993. Origin of turbulence – Producing eddies in a channel flow. Phys. Fluids A 5, 1011–1022.

Choi, H., Moin, P., Kim, J., 1992. Turbulent drag reduction: Studies of feedback control and flow over riblets. Rep. TF–55, Department of Mechanical Engineering, Stanford University.

Choi, H., Moin, P., 1994. Effects of the computational time step on numerical solutions of turbulent flow. J. Comput. Phys. 113, 1–4.

Choi, H., Moin, P., Kim, J., 1994. Active turbulence control for drag reduction in wall-bounded flows. J. Fluid Mech. 262, 75–110.

Chorin, A.J., 1969. On the convergence of discrete approximations to the Navier–Stokes equations. Math. Comput. 23, 341–353.

Jacobi, A.M., Shah, R.K., 1995. Heat transfer surface enhancement through the use of longitudinal vortices: A review of recent progress. Exp. Thermal Fluid Sci. 11, 295–309.

Jiménez, J., Moin, P., 1991. The minimal flow unit in near-wall turbulence. J. Fluid Mech. 225, 213–240.

Jung, W.J., Mangiavacchi, N., Akhavan, R., 1992. Suppression of turbulence in wall-bounded flows by high-frequency spanwise oscillations. Phys. Fluids A 8, 1605–1607.

Kasagi, N., Sumitani, Y., Suzuki, Y., Iida, O., 1995. Kinematics of the quasi–coherent vortical structure in near-wall turbulence. Int. J. Heat Fluid Flow 16, 2–10.

Kasagi, N., Shikazono, N., 1995. Contribution of direct numerical simulation to understanding and modelling turbulent transport. Proc. Roy. Soc. London Ser. A 451, 257–292.

Kim, J., Moin, P., 1985. Application of a fractional-step method to incompressible Navier–Stokes equations. J. Comput. Phys. 59, 308–323.

Kim, J., Moin, P., Moser, R., 1987. Turbulence statistics in fully developed channel flow at low Reynolds number. J. Fluid Mech. 177, 133–166.

Moin, P., Spalart, P.R., 1989. Contributions of numerical simulation data bases to the physics, modeling, and measurement of turbulence. In: George, W.K., Arndt, R. (Eds.), Advances in Turbulence, Hemisphere, New York, pp. 11–38.

Robinson, S.K., 1991. The Kinematics of Turbulent Boundary Layer Structure. NASA TM–103859.

Rosenfeld, M., Kwak, D., Vinokur, M., 1991. Fractional step solution method for the unsteady incompressible Navier–Stokes equations in generalized coordinate systems. J. Comput. Phys. 94, 102–137.

Smith, C.R., Metzler, S.P., 1983. The characteristics of low-speed streaks in the near-wall region of a turbulent boundary layer. J. Fluid Mech. 129, 27–54.

Temam, R. 1984. Navier–Stokes Equations, 3rd ed. North-Holland, New York, pp. 395–426.

Webb, R.L. 1987. Enhancement of single-phase heat transfer. In: Kakaç, S., Shah, R.K., Aung, W. (Eds.), Handbook of Single-Phase Convective Heat Transfer, Wiley, New York, pp. 17.1–17.62.